Modelling Fluid-Rock Interaction Induced by the Percolation of CO_2-Enriched Solutions in Core Samples: The Role of Reactive Surface Area

É. Brosse[1], C. Magnier[1] and B. Vincent[1]

1 Institut français du pétrole, Geology-Geochemistry Division, 1 et 4, avenue de Bois-Préau, 92852 Rueil-Malmaison Cedex - France
e-mail: etienne.brosse@ifp.fr

Résumé — **La modélisation des interactions eau-roche induites par la percolation de solutions enrichies en CO_2 dans des échantillons de carottes : le rôle de la surface réactive** — Comprendre le devenir du dioxyde de carbone (CO_2) injecté dans des aquifères ou des gisements d'hydrocarbures exploités reposera en partie sur l'utilisation de modèles chimie-transport, capables de prédire les interactions possibles entre les eaux acidifiées et les minéraux. Les résultats fournis par de tels modèles dépendent d'un grand nombre d'hypothèses et de paramètres, parfois mal contraints. Un aspect clé est l'intégration, dans les simulations portant sur des roches, de vitesses de réaction mesurées sur des minéraux apprêtés et isolés, et avec des rapports eau-roche beaucoup plus élevés.

Cet article est consacré à la modélisation d'expériences de percolation réactive, qui ont été mises au point pour améliorer l'intégration des vitesses de réaction. Ces expériences ont été menées sur des échantillons de calcaire naturel purement constitués de calcite (Noiriel *et al.*, ce volume), dans des conditions de température, de pression, de pression partielle de CO_2 (pCO_2) et de composition d'eau pour lesquelles une vitesse de dissolution de la calcite est disponible (Plummer *et al.*, 1978, modèle dit *PWP*). Ainsi, un modèle chimie-transport peut être utilisé pour simuler les expériences et pour discuter, précisément, la manière de transposer à la roche le modèle cinétique du minéral.

La comparaison entre les résultats expérimentaux et les résultats de calcul ne permet pas de décider du contrôle de la réaction de dissolution du calcaire, dans les conditions étudiées : soit la réaction de surface, soit un mécanisme de transport d'espèce(s) dans la phase aqueuse. Dans le premier cas, la démarche consiste à ajuster la valeur d'une surface dite « réactive ». Dans le second cas, le paramètre d'ajustement est l'épaisseur moyenne d'une couche diffuse, qui dépend du pH.

Abstract — *Modelling Fluid-Rock Interaction Induced by the Percolation of CO_2-Enriched Solutions in Core Samples: The Role of Reactive Surface Area* — *Understanding the fate of CO_2 disposed in aquifers or depleted hydrocarbon fields is partly based on the use of reaction-transport models, able to predict the possible interaction between acidified waters and the minerals. The results delivered by such models depend on many parameters and hypotheses, of which some are still poorly constrained. A key issue is how to transpose kinetics of a mineral reaction to a representative rock system, from data acquired in laboratory experiments involving controlled mineral powders under high water-to-mineral ratio.*

The paper focuses on the simulation of plug-flow experiments designed to improve the upscaling of kinetic rates. The experiments were performed on a natural limestone made of pure calcite (Noiriel et al., this issue), in conditions of temperature, pressure, pCO$_2$ and water composition for which a kinetic rate of dissolution is available for calcite (Plummer et al., 1978, the so-called PWP model). A reaction-transport code is used to simulate the experiment and then to investigate the transposition of the kinetic rate from the mineral to the rock material.

However, the comparison between experimental and modelling results cannot help to understand what is the main control on the dissolution rate of limestone in the conditions studied, either the surface reaction or a transport mechanism in the water phase. In the first case, a value of the reactive surface area must be adjusted. In the second case, the fitting parameter is the average thickness of a diffusive layer, which depends on pH.

INTRODUCTION

It is commonly believed that the disposal of carbon dioxide in saline aquifers or depleted hydrocarbon reservoirs leads to water-rock interaction. Carbon dioxide (CO_2) is highly soluble in hydrocarbon (*e.g.*, Simon and Graue, 1965; Vengu, 1983; Chung *et al.*, 1988) and also, though relatively less, in water (*e.g.*, Enick and Klara, 1990; Duan and Sun, 2003; Kervévan *et al.*, this issue, Portier and Rochelle, in press). When CO_2 dissolves in water, it forms the quantitatively dominant solvated molecule CO_2(aq) and the carbonic acid H_2CO_3 molecule (*e.g.*, Stumm and Morgan, 1970; Usdowski, 1982). H_2CO_3 partly dissociates to bicarbonate HCO_3^- and carbonate CO_3^{2-} ions, shifting pH towards a lower value (*e.g.*, Drever, 1997). The increased activity of proton, (H^+), promotes the dissolution of most of the minerals, which, in turn, liberates metal cations in the aqueous solution. Some of them can combine with bicarbonate or carbonate to precipitate mineral carbonates.

The work presented here aims at better integrating water-rock interaction modelling in the appraisal of CO_2 fate after injection. Two geochemical issues are of general concern to CO_2 storage in the subsurface. The first one is the assessment of the storage capacity created by the dissolution process coupled with the precipitation of secondary carbonates. A useful but simplistic approach to the problem is to consider only thermodynamics. Except in natural fields of carbon dioxide, the values of CO_2 partial pressure (noted pCO_2) observed in sedimentary basins or inferred from the equilibrium of mineral assemblages likely to be present (*e.g.*, Smith and Ehrenberg, 1989; Hutcheon and Abercrombie, 1990; Coudrain-Ribstein *et al.*, 1998) are much lower than the pCO_2 values that can be reached after injection for the purpose of storage. It means that injected CO_2 has the capacity to alter the mineral composition of the reservoir. When minerals containing cations which are able to combine with CO_3^{2-} to form mineral carbonates, are present and subsequently dissolve, there is a possibility that a part of the injected gas may change to solid phases. Assuming that a volume of host rock will react with a given amount of carbon dioxide at fixed temperature and pressure in an aqueous

solution of known initial composition, the composition of the system at equilibrium can be calculated and the transfer of carbon from the fluid phases to the mineral phases can be deduced. Bachu *et al.* (1994) and Gunter *et al.* (1993, 1997) showed that the capacity of a rock to convert a part of the injected carbon to carbonates, a mechanism known as "mineral trapping", is likely significant when at least two conditions are met:

– the rock composition is rich in alumino-silicates, particularly of the Fe-rich or Mg-rich varieties;
– the carbon is transported by a relatively efficient hydrodynamism (*e.g.*, 10 cm·y^{-1}).

Introducing kinetic rates of heterogeneous reactions allows determination of transient responses of the system and of the reaction path towards equilibrium. For example Gunter *et al.* (1997) presented batch experiments where mineral assemblages react at 105°C with CO_2-rich aqueous solutions. Due to slow rates, they did not observe the transformation of alumino-silicates (feldspars, micas) but they noted an evolution of the water composition. They interpreted the results using geochemical software with a formalism for kinetics. As carbonates react much more rapidly than alumino-silicates, an initial episode of calcite dissolution and of alkalinity increase precedes the production of divalent cations from alumino-silicates. In the long term, however, there is a significant conversion of CO_2 to calcite and siderite, *i.e.*, some mineral trapping. Finally, the question of mineral trapping is far from being accurately predicted today, as main controls of the phenomenon should combine the precipitation kinetics and the composition (*i.e.*, the formation of solid solutions) of the mineral phase(s) that must precipitate in order to accomodate the less soluble elements, in particular aluminum and iron.

A second geochemical issue concerns non desirable effects related to the reactivity of dissolved CO_2 with minerals. Dissolution, expected for carbonates, could weaken the injection zone. Later, it could favor the opening of cemented fractures in the caprock and lead to gas leakage. In contrast, a massive cementation near the injection zone could hamper injectivity. Some of these phenomena are mentioned in papers dedicated to CO_2-enhanced oil recovery (CO_2-EOR),

either from experimental study on plugs or from field observation. Ross *et al.* (1982) made flow-through experiments on calcite-rich sandstones and confirmed the dissolution of calcite. Mathis and Sears (1984) reported the dissolution of anhydrite in a dolomitic reservoir. Svec and Grigg (2001) observed both dissolution and precipitation of carbonates during water-alternate-gas (WAG) experiments in plugs. In all cases, kinetics of water-rock interaction determines the timing and scale of the phenomenon.

Rates of mineral dissolution and precipitation are generally derived from experiments performed on selected and prepared mineral grains, in mixed-flow reactors with strong stirring and high solution-to-solid ratio (for general considerations on open reactors see for instance Chou and Wollast, 1985; Mast and Drever, 1987; Dove and Crerar, 1990; Nagy *et al.*, 1990; Schnoor, 1990; Nagy *et al.*, 1991; Nagy and Lasaga, 1992; Burch *et al.*, 1993; Devidal *et al.,* 1997; Tester *et al.*, 1994). For reactions governed by surface mechanism the rate is calculated from the variation of an aqueous concentration between the inlet and the outlet of the reactor during well chosen steady-state experimental series, and from an assumption on the surface area that controls the process. The nature of the surface that represents more realistically the reactive surface of the mineral depends on the type of mineral, temperature and other experimental conditions. An adequate choice of surface is a matter of debate (*e.g.*, Gautier *et al.,* 2001; Jeschke and Dreybrodt, 2002; Lüttge *et al.,* 2003). However, in order to derive a prediction on geological systems, the combination of an experimental reaction-rate constant with the same type of surface area as used for interpreting the experiment should provide a correct estimation, as long as the mechanism that controls kinetics is the same.

However, further complexities arise from the fact that the mechanisms controlling kinetics can vary when passing from minerals in experiments to rocks in geological systems. In this case the formalism used for representing kinetics has to be adapted to the application of interest. In a stirred flow reactor the surface-reaction mechanism can govern kinetics, whereas in a rock, stagnant fluid around minerals and low solution-to-solid ratio may considerably enhance the role of diffusion (*e.g.*, Berner, 1978; Casey, 1987; Lichtner, 1996). Experiments made with a rotating disk (*e.g.*, Guy and Schott, 1989; Alkattan *et al.*, 1998) are able to distinguish the role of diffusion from the bulk kinetic rate. However, from one point of a rock sample to the other, the hydrodynamic conditions can vary to a large extent. Even in a very active hydrodynamic flow, the heterogeneous pore network guides the flow along particular pathways where the transfers of dissolved elements can occur, whereas in poorly connected regions, or pore dead-ends, stagnant aqueous solution can eventually attain different saturation states with respect to the minerals. Moreover, heterogeneities exist at all scales of a sedimentary rock, from the core-scale sample to the stratigraphic formation. In addition, several fluid phases can coexist in the pore space of the reservoir, *i.e.*, gas and water phases, eventually an oil phase. The wettability of the various minerals and the distribution of saturations add much complexity to the description of the sediment in terms of kinetic behaviour with respect to water-rock interaction.

Another aspect to consider for understanding reactions in a rock, is that the mineral surfaces are natural, in contrast with the prepared surfaces of powder material used for kinetic experiments. Natural surfaces present badly constrained geometries and a concentration of impurities that strongly influence kinetics and that should be studied specifically (*e.g.*, Eisenlohr *et al.*, 1999).

Predicting CO$_2$ fate and rock behaviour during CO$_2$ sequestration requires that reaction-transport numerical models can be used with a sufficient level of confidence. Despite progress in recent years (*e.g.*, Lichtner, 1996; Steefel and MacQuarrie, 1996; Xu *et al.*, 2003; Johnson *et al.,* 2004) such models still need to take more closely the geological reality into account. As mentioned above, one difficulty is how to integrate reaction rates, known for individual minerals, into the rock system (*e.g.*, White and Brantley, 2003, for a review). In order to provide better constrained rules to this puzzling choice, a first step is to perform reaction-transport experiments on relatively simple and well-known material, and to numerically simulate these experiments (*e.g.*, Johnson *et al.*, 1998; Kieffer *et al.*, 1999; Jové Colón *et al.*, 2004).

In the present paper we report simulations of flow-through experiments performed in well controlled temperature, pressure, chemical and hydrodynamic conditions on a pure natural limestone (details in Noiriel *et al.*, this issue). At the experimental conditions the rate law for the dissolution and precipitation of powder calcite grains is known from laboratory experiments made on individual minerals (PWP model, see Plummer *et al.*, 1978; Busenberg and Plummer, 1986). The simulations were made with a reaction-transport code able to account for the coupling between heterogeneous reactions (here, the dissolution of calcite) and the transport of dissolved elements in aqueous solution. The model also considers a reactive surface area for the mineral grains, which in the PWP model is derived from a geometric surface area. In order to fit the experimental measurements of effluent composition, the value of the reactive surface area must be adjusted to only a fraction of the calculated (or estimated) geometric surface area. The adjustment obtained is discussed as a function of the porosity of the rock, using published results on pure quartz rocks or agregates (Johnson *et al.*, 1998; Kieffer *et al.*, 1999; Jové Colón *et al.*, 2004). In a second part of the discussion the authors examine the consequence of a possible control of the diffusion of aqueous species close to the dissolving mineral, on the dissolution kinetics of calcite (Dreybrodt, 1981; Baumann *et al.*, 1985; Buhmann and Dreybrodt, 1985a, 1985b; Alkattan *et al.*, 1998).

Experimental conditions were chosen in such a way that, when the kinetic control of calcite dissolution was assumed to be the surface reaction mechanism, geochemical modelling could be used for appraising the reactive surface area involved in the reaction. The sample was selected because the crinoidal limestone is made of a unique mineral, calcite (*Section 1.1*) and because the petrophysical characters permit both an efficient reactive percolation and a 3D-imagery through synchrotron microtomography (Noiriel *et al.*, this issue). Temperature and pCO_2 were fixed at values where the PWP model of calcite dissolution kinetics is applicable (*Section 2.3*). The flow-rate value was set high enough to neglect dissipation (*Section 2.4*).

1 EXPERIMENTAL DATA

The experimental procedure and results obtained from the studied carbonate are documented in detail by Noiriel *et al.* (this issue). Some additional information on the petrological features observed before and after the experiment are given (*Section 1.1*), as well as a short overview of the experimental procedure (*Section 1.2*).

1.1 Crinoidal Limestone

The studied natural carbonate is a crinoidal limestone (crinoidal grainstone according to Dunham's classification) of middle Oxfordian age (*Plicatilis* biozone) sampled from the Lérouville quarry in the Paris Basin. Figure 1 shows typical sections observed by optical microscopy and scanning electronic microscopy (SEM). The main components of this limestone are crinoidal ossicles (echinoderma fragments). These clasts correspond to microporous single calcite crystals, initially in HMC (high magnesian calcite) but all recrystallized in LMC (low magnesian calcite) as demonstrated by SEM-associated microprobe (*Fig. 1, photo 3*). Most of the ossicles present a syntaxial overgrowth in lattice continuity with the host crystals (*Fig. 1*). These overgrowths are clear and inclusion free, which means a LMC precipitation initiated during mesogenesis.

The Lérouville grainstone also displays internal micritic and microbioclastic sediments with molds of previously micritized bioclasts (*Figs. 2a*). The micritic part accounts for few percent (5% maximum) of the limestone (image analysis). Part of this microcrystalline LMC has undergone
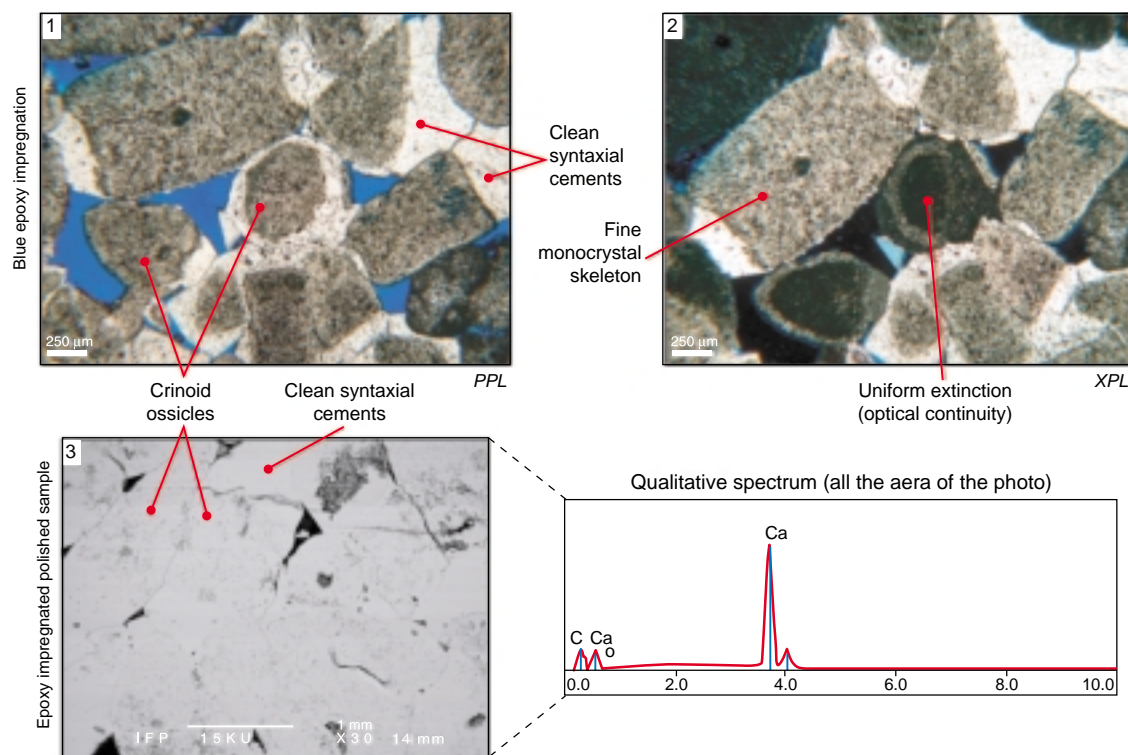

Figure 1

Petrographic observations of the Lérouville crinoidal limestone. Optical microscopy on thin sections (photos 1 and 2) allows to clearly identify the crinoid ossicles, corresponding to microporous single calcite crystals (uniform extinction; photo 2), and the syntaxial overgrowths in lattice continuity (photo 2). Scanning electronic microscopy (SEM) investigation in the back-scattered mode shows an uniform low magnesian calcite (LMC) mineralogy (photo 3 and associated spectrum).
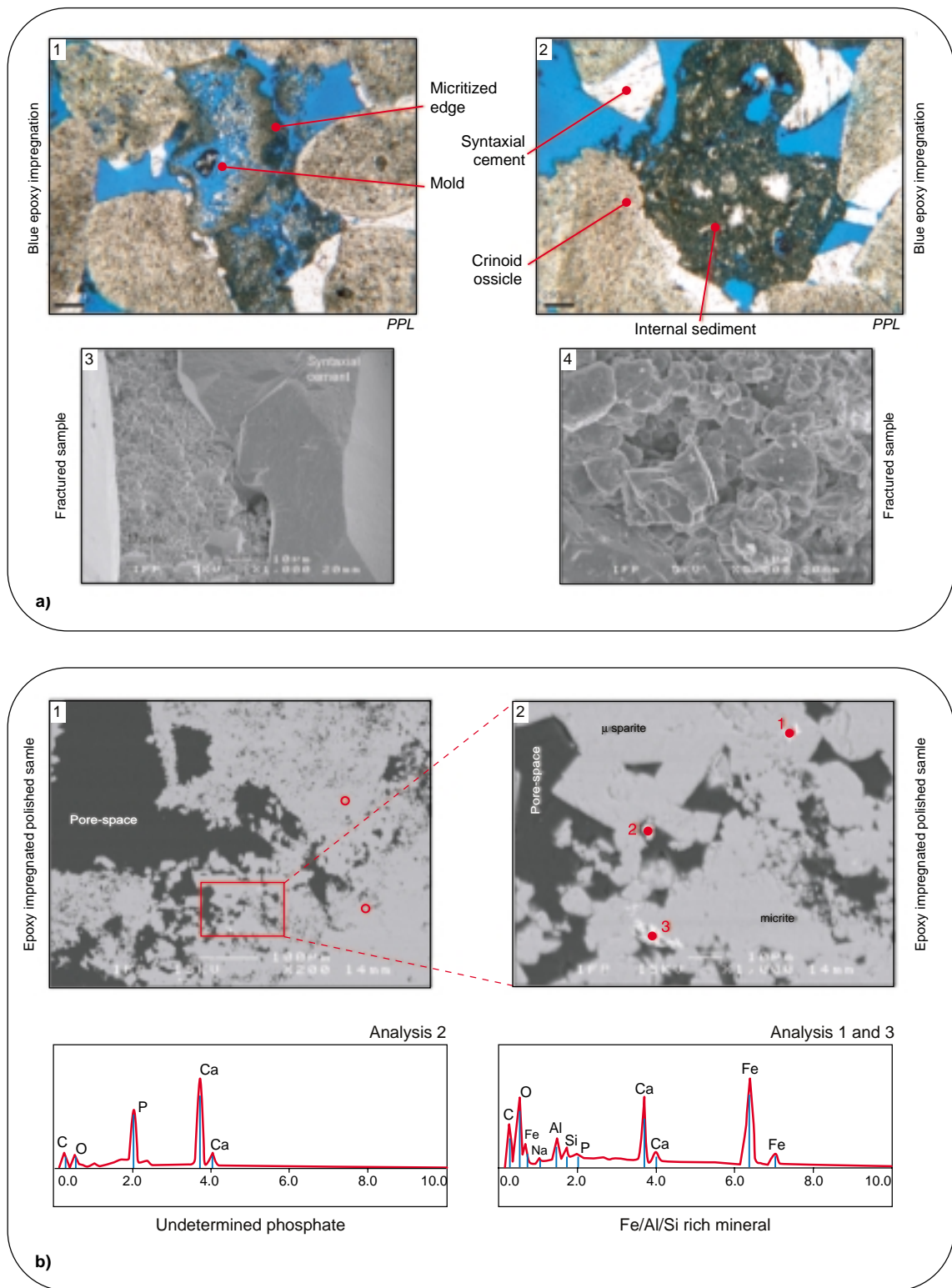
Figure 2

Microcrystalline calcite (micrite) in the Lérouville Limestone. a) Petrographic characteristics. Photo 1: mold of micritized bioclast (*sensu* Bathurst, 1975). Photo 2: micritic/microbioclastic internal sediment filling the primary interparticle pore-space. Photo 3: unmodified micrite with subhedral crystals. Photo 4: detail of dissolved anhedral crystals (amiboid shape). b) Chemical characteristics. SEM investigation in the back-scattered mode shows chemically contrasted particles within the LMC micrite (white spots; photos 1 and 2), corresponding to phosphor rich and iron/aluminium/silicium rich minerals.

dissolution *(Fig. 2a, photo 4)* which implies a flow of aggressive meteoric waters in the limestone, most probably during telogenesis according to the regional geodynamic setting (Tertiary stripping of the series in the Paris Basin). Within the micrite, rare Fe/Al/Si rich (altered clay?) and *P* rich minerals were recognized *(Fig. 2b)*. They are probably responsible for the macroscopic ochre colour of the micritic zones.

The porosity (Φ) of the Lérouville limestone was measured or estimated using various techniques. Image analysis from SEM images or from thin sections (optical microscopy) gives 8.3%. Brine porosity is 15%. The porosity provided by Hg-porosimetry is 14.1%. The curves obtained from Hg-porosimetry are shown in Figure 3. They indicate two distinct sets of pore size, each one accounting for approximately one half of the total porosity. The largest pores (pore-throat size *ca.* 80 µm) coincide with the inter-bioclast and/or inter-syntaxial cement spaces. They are quickly invaded and correspond to the porosity estimated through image analysis. Additionally, a smaller pore network (pore-throat size *ca.* 1 µm) needs a higher pressure to be invaded. It corresponds to inter-crystalline pores within micritic zones and to the non occluded intra-echinoderma skeleton porosity. A surface area between 0.1 and 0.2 $m^2 \cdot g^{-1}$ was measured by the BET method (Brunauer *et al.*, 1938), using nitrogen as the absorbing gas species. The air permeability measured in the sample used for core-flood experiments is 40 mD.

1.2 Flow-Through Experiments

Initially the sample (called ENT1P) was saturated with water containing dissolved 0.1 mol $CaCl_2$ and in equilibrium with calcite and atmosphere. Three successive episodes of water flow were carried out at 25°C and a pCO_2 value of 0.1 MPa (Table 1 in Noiriel *et al.*, this issue):

– episode 1 during 1 h 24 min with fresh water containing a low $CaCl_2$ amount, at a flow rate (q_{inj}) value of 300 $cm^3 \cdot h^{-1}$ (8.33×10^{-8} $m^3 \cdot s^{-1}$) (the composition reported in Table 1 represents the best fit obtained with available analysis);

– episode 2 during 12 h 30 min with deionized water, at a q_{inj} value of 300 $cm^3 \cdot h^{-1}$ (8.33×10^{-8} $m^3 \cdot s^{-1}$);

– epsiode 3 during 8 h 30 min with deionized water containing 0.01 mol NaCl, at a q_{inj} value of 100 $cm^3 \cdot h^{-1}$ (2.78×10^{-8} $m^3 \cdot s^{-1}$).

The pressure was continuously measured at the inlet and at the outlet, so that the evolution of permeability (K) could be deduced: 40 mD (initial), 300 mD (end episode 1), higher than 5 D (end episode 2). At each stage between two flow-through episodes the porous network of the sample was studied by X-ray computed microtomography at the *European Synchrotron Reasearch Facility* (ESRF) in Grenoble, as described in the cited article.

The composition of interstitial solution, either in place before percolation (initial stage), injected at the sample inlet (onset of any episode), or escaped at the outlet (every hour), was speciated by the DIAPHORE geochemical code (see *infra*). The computed composition is reported in Table 1. Experimental results are shown in figures presented later. At the considered dilution the extended Debye-Hückel's (B-dot) and Helgeson's formalisms used to calculate the activities of aqueous species are valid (Helgeson, 1969; Helgeson *et al.*, 1981).
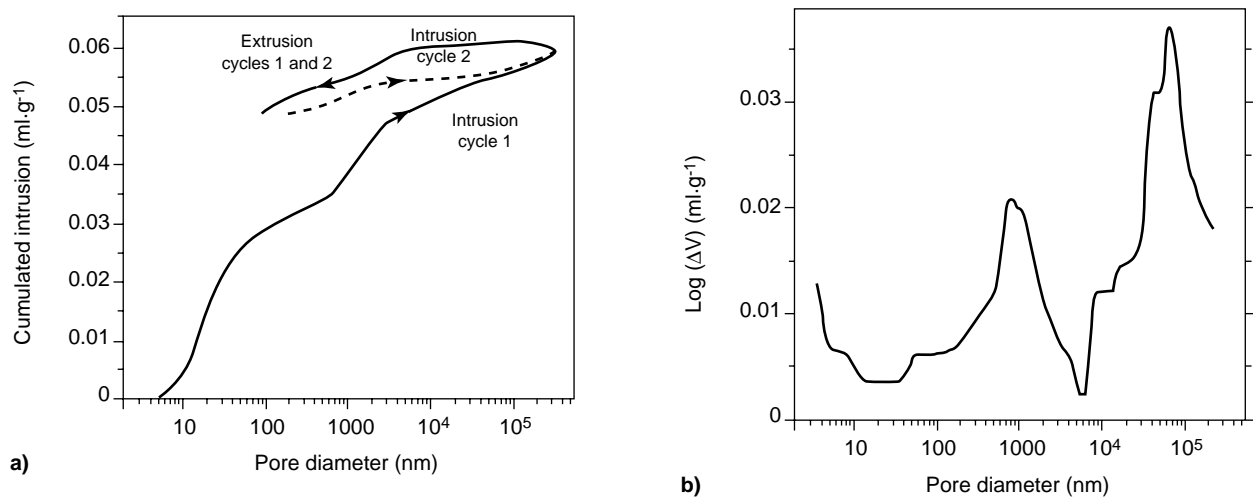

a)

b)

Figure 3

Hg-porosimetry of the crinoidal limestone. a) Drainage-imbibition-drainage successive episodes of the Hg-porosimetry procedure (the drainage corresponds to the intrusion of the nonwetting mercury phase into the air-impregnated sample). b) Distribution by pore-throat size.

TABLE 1

Composition of the solutions involved in the flow-through experiments of ENT1P, and petrophysical properties.
The reported values are computed values (DIAPHORE) that provide the best fit with the analytical data of Noiriel *et al.* (this issue)

Stage / rate	Percolation episode	Description/time from the onset of the designed episode	Cumulated time (h)	pH	Cl mol/kgH$_2$O	Na mol/kgH$_2$O	Ca mol/kgH$_2$O	Mg mol/kgH$_2$O	C mol/kgH$_2$O	Activity (Ca^{2+})	Activity (CO_3^{2-})	Activity (HCO_3^-)	Q $(Ca^{2+})\cdot(CO_3^{2-})$ Saturation/calcite	log Q/K	Calcite Crinoids vol%	Calcite Micrite vol%	Porosity (calculated) vol%	Permeability mD
Stage 0 (initial)	1	Equil. with carbonate	In situ	7.36	2.019×10^{-1}	1.011×10^{-6}	1.011×10^{-1}	1.011×10^{-6}	2.151×10^{-4}	3.010×10^{-2}	1.315×10^{-7}	9.480×10^{-5}	3.388×10^{-4}	0	84.00	1.00	15.00	40
300 cm^3·h^{-1}	1	Injected	Inlet	4.80	2.212×10^{-4}	5.700×10^{-6}	5.900×10^{-1}	2.300×10^{-5}	3.549×10^{-2}	4.826×10^{-4}	2.935×10^{-9}	9.718×10^{-4}	1.416×10^{-12}	-3.379	83.75	0.74	15.51	44
	1	1 h	1 / Outlet	5.13	2.217×10^{-4}	5.711×10^{-6}	1.183×10^{-3}	2.305×10^{-5}	3.617×10^{-2}	8.934×10^{-4}	1.304×10^{-8}	2.034×10^{-3}	1.165×10^{-11}	-2.464	83.50	0.25	15.98	49
	1	2 h	2 / Outlet	5.10	2.217×10^{-4}	5.711×10^{-6}	1.125×10^{-3}	2.305×10^{-5}	3.611×10^{-2}	8.554×10^{-4}	1.174×10^{-8}	1.932×10^{-3}	1.005×10^{-11}	-2.528				
Stage 1 — 300 cm^3·h^{-1}	2	Injected	Inlet	4.80	1.000×10^{-6}	1.000×10^{-6}	5.108×10^{-4}	1.000×10^{-6}	3.583×10^{-2}	4.264×10^{-4}	2.935×10^{-9}	9.922×10^{-4}	1.251×10^{-12}	-3.433				
	2	Starting time	2 / Outlet	5.10	2.222×10^{-4}	5.724×10^{-6}	1.127×10^{-3}	2.309×10^{-5}	3.619×10^{-2}	8.659×10^{-4}	1.152×10^{-8}	1.947×10^{-3}	9.977×10^{-12}	-2.531	83.50	0.00	16.50	52
	2	1 h	3 / Outlet	5.07	6.499×10^{-7}	1.002×10^{-6}	9.669×10^{-4}	1.002×10^{-6}	3.636×10^{-2}	7.571×10^{-4}	9.980×10^{-9}	1.820×10^{-3}	7.556×10^{-12}	-2.652	83.12		16.88	56
	2	2 h	4 / Outlet	5.07	6.499×10^{-7}	1.002×10^{-6}	9.655×10^{-4}	1.002×10^{-6}	3.636×10^{-2}	7.562×10^{-4}	9.952×10^{-9}	1.818×10^{-3}	7.526×10^{-12}	-2.653	82.75		17.25	60
	2	3 h	5 / Outlet	5.07	6.499×10^{-7}	1.002×10^{-6}	9.641×10^{-4}	1.002×10^{-6}	3.636×10^{-2}	7.552×10^{-4}	9.925×10^{-9}	1.815×10^{-3}	7.496×10^{-12}	-2.655	82.37		17.63	65
	2	4 h	6 / Outlet	5.07	6.499×10^{-7}	1.002×10^{-6}	9.628×10^{-4}	1.002×10^{-6}	3.636×10^{-2}	7.543×10^{-4}	9.898×10^{-9}	1.813×10^{-3}	7.466×10^{-12}	-2.657	82.00		18.00	69
	2	5 h	7 / Outlet	5.07	6.499×10^{-7}	1.002×10^{-6}	9.614×10^{-4}	1.002×10^{-6}	3.636×10^{-2}	7.534×10^{-4}	9.871×10^{-9}	1.810×10^{-3}	7.436×10^{-12}	-2.659	81.63		18.37	74
	2	6 h	8 / Outlet	5.06	6.499×10^{-7}	1.002×10^{-6}	9.600×10^{-4}	1.002×10^{-6}	3.636×10^{-2}	7.524×10^{-4}	9.843×10^{-9}	1.808×10^{-3}	7.406×10^{-12}	-2.660	81.26		18.74	79
	2	7 h	9 / Outlet	5.06	6.499×10^{-7}	1.002×10^{-6}	9.587×10^{-4}	1.002×10^{-6}	3.636×10^{-2}	7.515×10^{-4}	9.816×10^{-9}	1.805×10^{-3}	7.377×10^{-12}	-2.662	80.89		19.11	85
	2	8 h	10 / Outlet	5.06	6.499×10^{-7}	1.002×10^{-6}	9.573×10^{-4}	1.002×10^{-6}	3.636×10^{-2}	7.505×10^{-4}	9.789×10^{-9}	1.803×10^{-3}	7.347×10^{-12}	-2.664	80.52		19.48	91
	2	9 h	11 / Outlet	5.06	6.499×10^{-7}	1.002×10^{-6}	9.560×10^{-4}	1.002×10^{-6}	3.635×10^{-2}	7.496×10^{-4}	9.763×10^{-9}	1.801×10^{-3}	7.318×10^{-12}	-2.666	80.15		19.85	97
	2	10 h	12 / Outlet	5.06	6.499×10^{-7}	1.002×10^{-6}	9.546×10^{-4}	1.002×10^{-6}	3.635×10^{-2}	7.486×10^{-4}	9.736×10^{-9}	1.798×10^{-3}	7.289×10^{-12}	-2.667	79.79		20.21	103
	2	11 h	13 / Outlet	5.06	6.499×10^{-7}	1.002×10^{-6}	9.533×10^{-4}	1.002×10^{-6}	3.635×10^{-2}	7.477×10^{-4}	9.709×10^{-9}	1.796×10^{-3}	7.260×10^{-12}	-2.669	79.42		20.58	110
	2	12 h	14 / Outlet	5.06	6.499×10^{-7}	1.002×10^{-6}	9.519×10^{-4}	1.002×10^{-6}	3.635×10^{-2}	7.468×10^{-4}	9.683×10^{-9}	1.793×10^{-3}	7.231×10^{-12}	-2.671	79.06		20.94	
Stage 2 — 100 cm^3·h^{-1}	3	Injected	Inlet	4.80	1.000×10^{-2}	1.000×10^{-2}	5.467×10^{-4}	1.000×10^{-6}	3.583×10^{-2}	3.578×10^{-4}	2.934×10^{-9}	9.919×10^{-4}	1.050×10^{-12}	-3.509				
	3	1 h	15 / Outlet	5.36	1.003×10^{-2}	1.003×10^{-2}	2.009×10^{-3}	1.003×10^{-6}	3.737×10^{-2}	1.218×10^{-3}	3.785×10^{-8}	3.495×10^{-3}	4.612×10^{-11}	-1.866	78.70		21.30	116
	3	2 h	16 / Outlet	5.36	1.003×10^{-2}	1.003×10^{-2}	2.004×10^{-3}	1.003×10^{-6}	3.737×10^{-2}	1.216×10^{-3}	3.766×10^{-8}	3.486×10^{-3}	4.579×10^{-11}	-1.869	78.30		21.70	124
	3	3 h	17 / Outlet	5.36	1.003×10^{-2}	1.003×10^{-2}	1.999×10^{-3}	1.003×10^{-6}	3.736×10^{-2}	1.213×10^{-3}	3.748×10^{-8}	3.478×10^{-3}	4.546×10^{-11}	-1.872	77.91		22.09	132
	3	4 h	18 / Outlet	5.36	1.003×10^{-2}	1.003×10^{-2}	1.994×10^{-3}	1.003×10^{-6}	3.736×10^{-2}	1.210×10^{-3}	3.730×10^{-8}	3.470×10^{-3}	4.514×10^{-11}	-1.875	77.51		22.49	140
	3	5 h	19 / Outlet	5.36	1.003×10^{-2}	1.003×10^{-2}	1.989×10^{-3}	1.003×10^{-6}	3.735×10^{-2}	1.208×10^{-3}	3.711×10^{-8}	3.461×10^{-3}	4.482×10^{-11}	-1.879	77.12		22.88	149
	3	6 h	20 / Outlet	5.36	1.003×10^{-2}	1.003×10^{-2}	1.984×10^{-3}	1.003×10^{-6}	3.735×10^{-2}	1.205×10^{-3}	3.693×10^{-8}	3.453×10^{-3}	4.450×10^{-11}	-1.882	76.72		23.28	159
	3	7 h	21 / Outlet	5.36	1.003×10^{-2}	1.003×10^{-2}	1.979×10^{-3}	1.003×10^{-6}	3.734×10^{-2}	1.202×10^{-3}	3.675×10^{-8}	3.445×10^{-3}	4.418×10^{-11}	-1.885	76.33		23.67	169
	3	8 h	22 / Outlet	5.36	1.003×10^{-2}	1.003×10^{-2}	1.974×10^{-3}	1.003×10^{-6}	3.734×10^{-2}	1.200×10^{-3}	3.657×10^{-8}	3.437×10^{-3}	4.387×10^{-11}	-1.888	75.94		24.06	179
	3	9 h	23 / Outlet	5.35	1.003×10^{-2}	1.003×10^{-2}	1.969×10^{-3}	1.003×10^{-6}	3.733×10^{-2}	1.197×10^{-3}	3.639×10^{-8}	3.429×10^{-3}	4.356×10^{-11}	-1.891	75.55		24.45	190
	3	10 h	24 / Outlet	5.35	1.003×10^{-02}	1.003×10^{-2}	1.964×10^{-3}	1.003×10^{-6}	3.733×10^{-2}	1.194×10^{-3}	3.621×10^{-8}	3.420×10^{-3}	4.324×10^{-11}	-1.894	75.16		24.84	201

2 MODELLING APPROACH

The modelling work presented in this article was achieved using DIAPHORE, a reaction-transport numerical code (Le Gallo *et al.,* 1998; Cassou, 2000). This model, developed for predicting diagenetic effects in reservoirs, considers a rock saturated with water. The heterogenous reactions, *i.e.,* dissolutions or precipitations of minerals, are described with kinetics. The formalism used for representing the reaction rates is detailed in Appendix A. The grain model is introduced in Section 2.2. The solubility of a gas component at fixed partial pressure and in equilibrium with the solution is calculated according to Henry's law and appropriate corrections (Portier, 2005; Portier and Rochelle, in press).

The user's inputs include:
– the geometry of the system and the size of the grid elements;
– the initial mineralogical composition;
– the initial distribution of porosity, permeability and grain-size values;
– the temperature;
– the composition of the solution initially present in the system, at equilibrium;
– the flow rate and the composition of the injected solution.

DIAPHORE restitutes the composition of the system (solution and minerals), porosity and permeability *vs* space and time.

2.1 Geometry of the System, Geochemical and Dynamic Parameters

The plug cylinder of crinoidal limestone has a 9 mm diameter and is 21 mm long. The system is represented by a regular 1D grid that was subdivided in 42 elements, each being 0.5 mm long. The raw input data include also the composition of the natural and injected solutions, initial petrophysical parameters and the flow-rate value.

The model calculated an initial water speciation at equilibrium with the mineral calcite at ambient temperature (25°C) and atmospheric pCO_2 (value of 3.0×10^{-4} bar) (*Table 1*). At equilibrium, the pH value of the computed water solution is 7.36. The successive aqueous solutions percolating through the rock were equilibrated at pH 4.8 and pCO_2 1 bar. Table 2 gives the speciation of these solutions and their alkalinity value. It also shows which aqueous species were taken into account by the geochemical model. An additionnal comment on the speciation is given in Section 2.3.

2.2 Grain Model and Surface Area

In the DIAPHORE numerical model minerals are represented by spheres. Their size varies as mineral reactions progress. This allows to account for variations of mineral surface and

permeability. A specific initial size is allocated to any type of grain. In the option chosen for the work presented here, the number of grains of each type remains unchanged. In addition, a mineral can be splitted in several grain types (for instance, here calcite was splitted in crinoidal grains and micrite grains). A choice of empirical relationships is available for deriving permeability from porosity, mineral-ogical composition and mineral surface area.

The first simulations were run considering that calcite grains have an average size diameter represented by a unique value. Several values were tested but none could give a satisfactory fit with measured Ca values at the outlet. A better fit was obtained when two classes of grain size were introduced, namely large grains of 300 μm initial diameter (echinoderma fragments), and small grains of 5 μm initial diameter (micrite). The main difference between a one grain *vs* a two grain model lies in the computed surface value that represents the reactive surface area offered for dissolution. A unique size to represent the calcite crystals, with porosity 15% and grain diameter 300 μm, renders a geometric surface area of 3.0×10^{-3} $m^2 \cdot g_{rock}^{-1}$. In contrast, if the limestone ($\Phi = 15\%$) is represented by A vol% of large grains (diameter 300 μm, A between 81 and 84) and B vol% of small ones (diameter 0.5 to 5 μm, B between 4 and 1), the value of geometric surface area ranges from 8.0×10^{-3} $m^2 \cdot g_{rock}^{-1}$ to 2.0×10^{-1} $m^2 \cdot g_{rock}^{-1}$, much closer to the measured BET surface area (*Section 1.1*). The ratio between the measured BET surface area and the geometric surface area calculated above, is consistent with the obvious imperfections of the model, that does not include either the steric aspects (the surface area of the whole sphere is considered), or the nonspherical character of many grains, or the "roughness" of the mineral surface (Withe and Peterson, 1990).

2.3 Thermodynamic Constants and Kinetic Rate for Calcite

The values of thermodynamic constants for the reactions considered are reported in Table 3, where they are compared to the values used by Plummer *et al.* (1978) for interpreting their kinetic experiments (see below). The value considered for the solubility product of calcite is consistent with the presence of $CaCO_3$ (aq) and $CaHCO_3^+$ in the speciation (Usdowski, 1982), as shown in Table 2.

The conditions of experiment through the Lérouville limestone (25°C, dilute solution, $pCO_2 = 1$ bar) were chosen in order for the reaction rates measured for calcite by Plummer *et al.* (1978) and Busenberg and Plummer (1986) to be applicable. The former paper documented the reaction kinetics of Iceland spar in the system H_2O-CO_2 between 5 and 60°C and in the pCO_2 range 0-1 bar. The latter completed the work, at 25°C, with data appropriate near equilibrium, and with the effect of salts (KOH, $KHCO_3$, alone or mixed; $Ca(HCO_3)_2$). The analyses made by these

TABLE 2

Aqueous speciation calculated for initial water and injected waters

Aqueous species	Molality (mol·kg$_{H_2O}^{-1}$)			
	0 *(in situ)*	0 (inlet)	1 (inlet)	2 (inlet)
H$_2$O	55.51	55.51	55.51	55.51
H$^+$	5.473 10^{-8}	1.657 10^{-5}	1.651 10^{-5}	1.743 10^{-5}
OH$^-$	3.278 10^{-7}	6.618 10^{-10}	6.669 10^{-10}	7.133 10^{-10}
Na$^+$	9.875 10^{-7}	5.697 10^{-6}	9.995 10^{-7}	9.984 10^{-3}
Cl$^-$	1.997 10^{-1}	2.212 10^{-4}	1.000 10^{-6}	9.989 10^{-3}
Ca^{2+}	9.990 10^{-2}	5.811 10^{-4}	5.059 10^{-4}	5.425 10^{-4}
Mg^{2+}	9.993 10^{-7}	2.285 10^{-5}	9.906 10^{-7}	9.919 10^{-7}
K$^+$	9.991 10^{-7}		1.000 10^{-6}	9.999 10^{-7}
S$_r^{2+}$		4.500 10^{-7}		
H$_2$CO$_3$	9.676 10^{-6}	3.447 10^{-2}	3.479 10^{-2}	3.469 10^{-2}
HCO$_3^-$	1.478 10^{-4}	1.019 10^{-3}	1.036 10^{-3}	1.105 10^{-3}
CO$_3^{2-}$	4.564 10^{-7}	3.547 10^{-9}	3.493 10^{-9}	4.535 10^{-9}
Alkalinity	1.487 10^{-4}	1.019 10^{-3}	1.036 10^{-3}	1.105 10^{-3}
NaCO$_3^-$	2.048 10^{-12}	3.112 10^{-13}	5.461 10^{-14}	5.445 10^{-10}
CaCO$_3$(aq)	6.697 10^{-6}	2.244 10^{-9}	2.656 10^{-9}	2.222 10^{-9}
CaHCO$_3^+$	4.806 10^{-5}	8.943 10^{-6}	4.922 10^{-6}	4.395 10^{-6}
MgCO$_3$(aq)	3.607 10^{-11}	1.405 10^{-10}	2.343 10^{-12}	1.866 10^{-12}
MgHCO$_3^+$	5.864 10^{-10}	1.543 10^{-7}	9.439 10^{-9}	8.050 10^{-9}
NaHCO$_3$(aq)	3.822 10^{-11}	2.968 10^{-9}	5.227 10^{-10}	4.874 10^{-6}
NaCl(aq)	1.244 10^{-8}	1.617 10^{-10}	1.292 10^{-13}	1.124 10^{-5}
HCl(aq)	1.187 10^{-9}	2.653 10^{-15}	3.241 10^{-12}	3.014 10^{-8}
Mg(OH)$^+$	4.396 10^{-11}	4.818 10^{-12}	2.135 10^{-13}	1.820 10^{-13}
Ca(OH)$^+$	1.339 10^{-7}	5.473 10^{-12}	3.970 10^{-12}	3.557 10^{-12}

authors were formalized in the PWP model (Plummer, Wigley and Parkhurst):

$$k_+(T) = k_1(H^+)_s + k_2(H_2CO_3^*)_s$$
$$+ k_3(H_2O)_s - k_4(Ca^{2+})_s \cdot (HCO_3^-)_s \quad (1)$$

where $(i)_s$ represents the activity of species i in the solution at the contact with the mineral surface, and $H_2CO_3^*$ represents $CO_2(aq) + H_2CO_3$. $k_+(T)$ is a notation adopted here to be consistent with Appendix A. In Section 4.2, we discuss possible differences existing between activity values at mineral surface, *i.e.*, $(i)_s$, and in the bulk solution, *i.e.*, (i). From now on, we consider that the two activities are equal. The three first terms in the right-hand side, in Equation (1) are called *forward* because they correspond to dissolution, whereas the last term is called *backward* (for precipitation). The PWP model provides expressions for the variation of k_1, k_2, k_3 *vs* temperature (Arrhenius' law), and a way to calculate k_4.

The PWP model was calibrated by Plummer *et al.* (1978) from experimental data on pure calcite, using geometric surface areas estimated from the mineral grains (rhombohedron shape assumed for the mineral grains obtained by crushing). To apply it in a different context, here a rock made also of pure calcite, the rate $k_+(T)$ must be multiplied by an estimation of the geometric surface area offered by the solution/mineral interface. In addition, it must be checked, or assumed, that the dissolution mechanism is the same.

In the range of compositions that concern the studied experiments *(Table 2)* the preceding considerations lead to a dependence on pH of the dissolution rate that is represented in Figure 4. As the formalism used for dissolution in the DIAPHORE model differs from the PWP formalism *(Eq. 1)*, its parameters *(Appendix A)* were adjusted to the following values: $pH_A^T = 4.7$; $n_A^T = 0.52$; $k_{d,A}^T = 1.0 \times 10^5$ mol·m^{-2}·y^{-1}; $k_{d,N}^T = 3.6 \times 10^2$ mol·m^{-2}·y^{-1}. These values, chosen to fit the
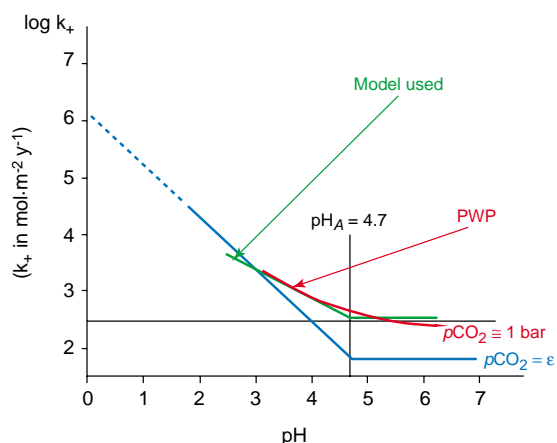
Figure 4

Dissolution kinetics of calcite. The model used, according to the formalism developed in Appendix A, is compared to the PWP model derived from experiments at pCO_2 1 bar.

TABLE 3

Thermodynamic data considered in the simulations
(system H_2O-CO_2-$CaCO_3$)

			DIAPHORE	PWP
$H_2O(aq) \leftrightarrow H^+ + OH^-$	$\log K_w$		-14.0	-13.992
$CO_2(g) \leftrightarrow CO_2(aq)$	$\log K_{H\text{-}1}$			-1.468
$CO_2(g) + H_2O \leftrightarrow H_2CO_3^\circ$	$\log K_{H\text{-}2}$		-1.46	
$CO_2(aq) + H_2O \leftrightarrow HCO_3^- + H^+$	$\log K_{1\text{-}1}$			-6.352
$H_2CO_3^\circ \leftrightarrow HCO_3^- + H^+$	$\log K_{1\text{-}2}$		-6.35	
$HCO_3^- \leftrightarrow H^+ + CO_3^{2-}$	$\log K_2$		-10.32	-10.329
$Ca^{2+} + HCO_3^- \leftrightarrow CaHCO_3^+$	$\log K_{CaHCO_3+}$		1.26	1.11
$Ca^{2+} + CO_3^{2-} \leftrightarrow CaCO_3^\circ$	$\log K_{CaCO_3}$		3.20	3.22
$Ca^{2+} + OH^- \leftrightarrow CaOH^+$	$\log K_{CaOH+}$		1.23	1.30
$CaCO_3(calcite) \leftrightarrow Ca^{2+} + CO_3^{2-}$	$\log K_C$		-8.47	-8.48

PWP model in the pH range of interest at 25°C (*T*) *(Fig. 4)*, are specific to the modelling work presented here. In the range of pCO_2 values obtained for the solution in the core during the percolation experiment this model predicts that calcite dissolves at a rate that ranges between 1.6×10^{-5} and 3.2×10^{-5} mol·m^{-2}·s^{-1}.

In order to complete the PWP model for precipitation, we also used the data of Dromgoole and Walter (1990). These data were adjusted by the formalism developed in Appendix A (*Eq. A7*), with $a_T = 1$, $b_T = 1.15$ and $\log k_-(25°C) = 1.8$ mol·m^{-2}·y^{-1}. However, in the conditions adopted for the flow-through experiment in the Lérouville limestone, either observations or simulations show that no calcite precipitation takes place.

2.4. Reaction *vs* Transport: Dominant Mechanism

Adimensional numbers are useful to analyse what part of the reaction-transport mechanism, namely reaction, advection, or dissipation (diffusion and dispersion), controls the evolution of the system considered. They are used here with respect to the concentration of Ca^{2+}. The scale of interest is the length of the plug, *i.e.*, 2.1×10^{-2} m. The pore volume of the plug is *ca.* 2.0×10^{-7} m^3. The residence time is 2.4 s and 7.2 s, respectively, for the considered injection rates q_{inj} (300 and 100 cm^3·h^{-1}). That corresponds to high fluid-flow velocities (v_{inj}), 8.75×10^{-3} m·s^{-1} and 2.92×10^{-3} m·s^{-1}, respectively. For such values hydrodynamic dispersion dominates molecular diffusion, as can be shown using the "diffusional Peclet number", Pe^* (Oelkers, 1996):

$$Pe^* = \frac{d.v_{inj}}{D^0} \quad (2)$$

where d represents the average grain diameter (m) and D^0 stands for the bulk molecular diffusivity of the considered element (m^2·s^{-1}). For Pe^* larger than 5, mechanical dispersion dominates molecular diffusion (Oelkers, 1996).

Considering the echinoderma fragments and taking 5×10^{-4} m for d and 1×10^{-9} m^2·s^{-1} for the coefficient D^0 of calcium (a standard value at 25°C), the Pe^* values that result from the two flow rates are, respectively, 4,375 and 1,458. For such high Pe^* values, the coefficient of longitudinal hydrodynamic dispersion (D_L) could be taken as follows (Oelkers, 1996):

$$D_L = D^0 \cdot \kappa \cdot (Pe^*)^{n_k} \quad (3)$$

with, for Pe^* greater than 100, $\kappa = 1.8$ and $n_\kappa = 1.0$. Here the D_L values are *ca.* 7.9×10^{-6} m^2·s^{-1} and 2.6×10^{-6} m^2·s^{-1}, respectively, much higher than the molecular diffusivity.

Considering now the grains of micrite (their presence was limited to the first flow-through episode, see *infra*) and taking 5×10^{-6} m for d the Pe^* value is close to 44. Mechanical dispersion still dominates molecular diffusion, but in Equation (3) $\kappa = 0.5$ and $n_\kappa = 1.2$ (Oelkers, 1996), and the D_L value is *ca.* 4.65×10^{-8} m^2·s^{-1}, almost 50 times higher than the molecular diffusivity.

Introducing the adimensional Peclet number (*Pe*) calculated from the coefficient D_L:

$$Pe = \frac{L.v_{inj}}{D_L} \quad (4)$$

where L is the length of interest, here the plug length 2.1×10^{-2} m, the *Pe* value is between 23 (large grain) and 3,952 (small grain). It shows that the transport is controlled by advection, and that dispersion can be neglected in the reaction-transport simulation.

Comparing now the relative importance of advective transport and reaction the adimensional Damköhler number *Da* (Knapp, 1989) can be used:

$$Da = \frac{\alpha \cdot S_r \cdot k_+(T) \cdot L}{C_{eq} \cdot v_{inj}} \quad (5)$$

where $\alpha = 1$ is the stoichiometric coefficient of Ca in calcite (CaCO₃). S_r represents the specific reactive surface area ($m^2_{mineral} \cdot m^{-3}_{solution}$). $k_+(T)$ stands for the dissolution rate constant of calcite at the temperature *T*, as described in Appendix A, here 1.6×10^{-5} to 3.2×10^{-5} mol·$m^{-2}_{mineral}$·s^{-1} in the concerned range of pH. C_{eq} is the concentration of Ca^{2+} at equilibrium with calcite, necessarily higher than 30 (*Table 2*: value for initial water) because injected water, with higher pCO_2 value, has a lower CO_3^{2-} molality value. Considering the lowest value estimated for S_r (*Section 2.2*) and the plug length for *L*, a maximum value of 0.94 is calculated for *Da*, that means kinetics plays an important role in the phenomenon. An *a posteriori* calculation, using DIAPHORE results, allows to check that the effluent water remains very undersaturated with respect to calcite, as indicated by the saturation index log *Q/K* (*Table 1*).

With the implicit scheme considered in DIAPHORE, the numerical dispersion can be expressed by the following coefficient D_{num}:

$$D_{num} = \frac{\Delta x \cdot v_{inj}}{2} \quad (6)$$

where Δx stands for the length of the grid element (here 5.0×10^{-4} m). With the values of v_{inj} considered in the experiment, numerical dispersion is slightly narrower than physical dispersion, since their respective values are *ca.* 2.2×10^{-6} m²·s⁻¹ and 7.3×10^{-7} m²·s⁻¹.

3 RESULTS OF SIMULATION, CRINOIDAL LIMESTONE

Figure 5 presents the best fit obtained when calcite was splitted in two grain types (*Section 2.2*). The parameters that influence dissolution and subsequent mineral constitution are:
– the proportion of large grains to small grains;
– the reactive surface area of each grain type.

Several choices are possible to adjust the reactive surface area from what is known of either the grains and pore geometry, or the plug-flow experiment. In the present work a surface correction (σ) was used as a fitting parameter, in order that the reactive surface area S_r of the rate law represents only a part of the geometric surface area S_{geom} defined from the grain model:

$$\sigma = \frac{S_r}{S_{geom}} \quad (7)$$

We imposed that the surface correction σ be the same for the two grain types, and, for a given rock type, change only (and slightly) with the porosity value. In that respect, the parameter σ appears to represent a sort of "accessibility" coefficient that measures the efficiency of the flowing fluid to reach the reactive sites of the mineral. Here a value of 0.15 was found for σ, and kept constant during the whole simulation.

In Figure 5 are represented three parameters calculated *vs* time by the simulation that provided the best fit with the experimental results:
– the vol% of calcite cumulated in the whole plug *(Fig. 5a)*;
– the total calcium content mol·$kg^{-1}_{H_2O}$ of the effluent water close to the plug outlet (grid element N. 42) *(Fig. 5b)*;
– its pH value *(Fig. 5b)*.

The composition measured from samples of the effluent solution is reproduced for comparison *(Fig. 5b)*.

A first remark is the effect of flow rate on water composition. As the flow-rate value drops from episode 2 to episode 3 the residence time of water increases, the reaction can come closer to equilibrium. The values of pH and dissolved calcium increase. The kinetic rate varies, not from the value of $k_+(T)$ that remains constant in the considered pH domain *(Fig. 4)*, but from the value of $\left(1 - \dfrac{Q}{K^T_{eq}}\right)$ *(Appendix A, Eq. A1)*.

During the first episode the micrite grains were completely dissolved. Figure 5 a shows that during the three water-flow episodes the dissolution of calcite computed by the model amounts respectively to 1.5, 4.4 and 3.5 vol%. These values must be compared to those reported in their Table 5 by Noiriel *et al.* (this issue), either from the effluent composition (0.3, 3.9 and 2.1 vol%, respectively), or from tomography on bulk sample (0.5, 4.0 and 3.5 vol%, respectively). The difference between experiment and simulation is mainly due to the mechanical migration of fine micrite particles, which of course was not represented in the geochemical model. In the simulation the proportion and grain size of micrite were adapted to obtain their complete dissolution at the end of episode 1.

The profiles of calcite abundance *vs* distance calculated by the model at various timesteps show that the dissolution process affects the whole core in an almost homogenous way. This results from the strong under-saturation of water with respect to the mineral *(Table 1)*.

Figure 6 presents some pictures of the core sample after the successive flow-through episodes that were described above. The flow of aggressive CO₂-charged water in the limestone dissolved calcite, especially on the edges of the macropores *(Fig. 6, photos 2 and 3)*. But the microporous crinoid ossicles are also affected by leaching around their central channels, *i.e.*, the former location of the crinoid tige *(Fig. 6, photos 4 and 5)*.
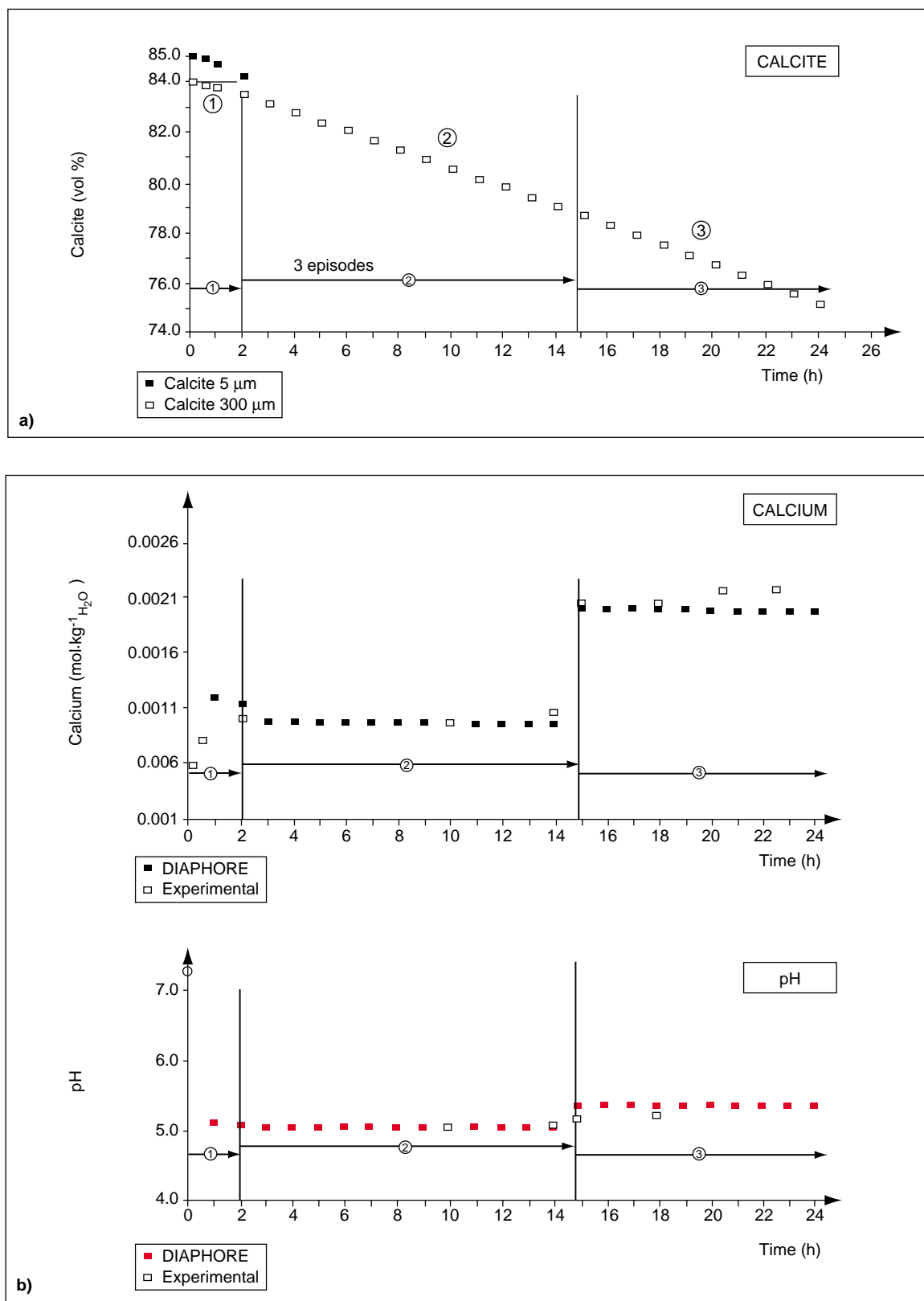
Figure 5

Simulation results *vs* time for the crinoidal limestone, and comparison with experimental results. a) Calcite vol%. The micrite grains were completely dissolved during episode 1. b) Total dissolved calcium and pH, computed and measured from the effluent.
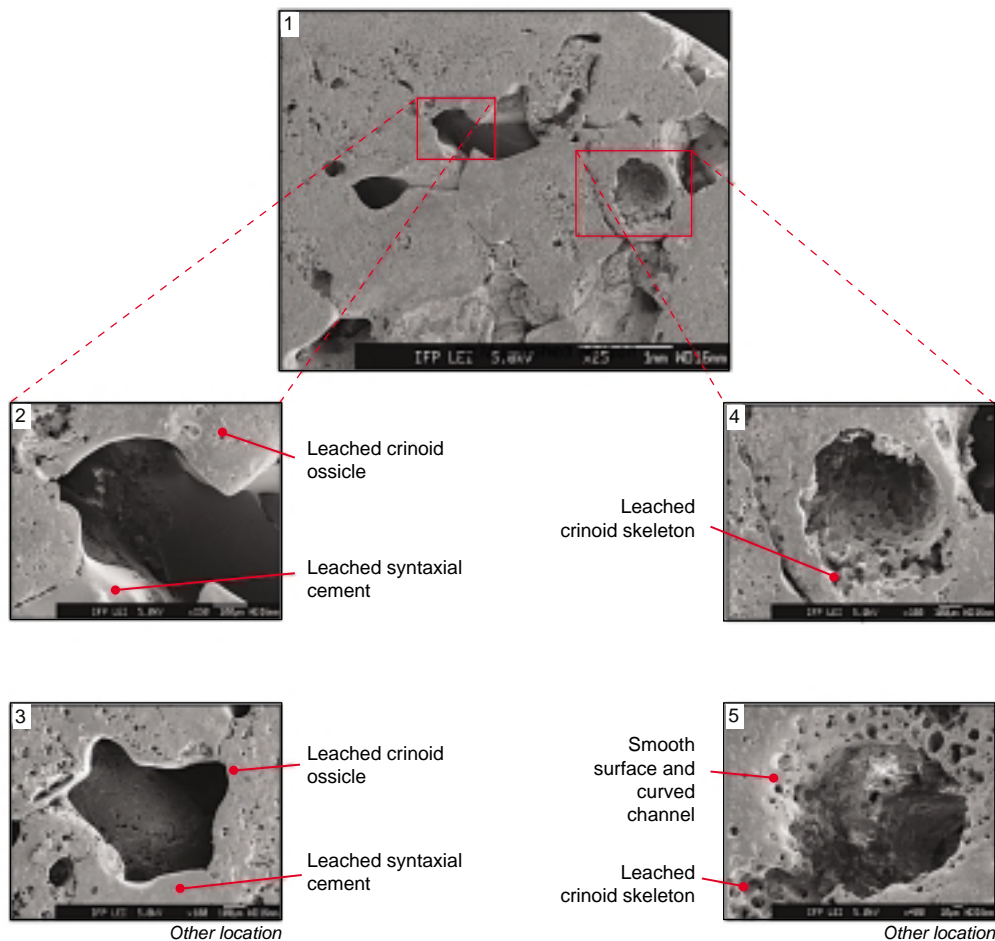
Figure 6

Effects of flow-trough on a Lérouville limestone plug. Various dissolution features are observed with SEM on polished section. Macropores are enlarged through leaching of both crinoid ossicles and syntaxial cements which are smoothed (photos 1, 2 and 3). The microporous crinoid skeleton is also greatly altered, especially around the central channels of the ossicles (photos 1, 4 and 5).

4 DISCUSSION

The flow-through experiment presented on the Lérouville crinoidal limestone (ENT1P) was designed in such a way that a well-known dissolution rate, the PWP's kinetics, could be used in the numerical simulation, only assuming that the kinetic control is the same for the calcite grains (PWP's experiments) and the limestone. With this assumption the model served to adjust (parameter σ) the reactive surface area offered by the mineral grains inside the rock core. The best adjustment was obtained with a two-grains model (initial state) and a σ value of 0.15. At the centimetre scale of investigation we interpreted σ as an accessibility parameter of the fluid to the reaction surface (*Eq. 7*, above). A first part of the discussion will consider the variation of σ with porosity.

A second aspect to discuss is the meaning of the reactive surface with respect to the mechanisms of the reaction. The PWP's kinetic rate is based on an interpretation of

experimental measurements that assumes a control of the reaction by the surface mechanism, and refers to an estimation of the geometric surface area. However, for calcite in the conditions of temperature and pH considered, a mixed kinetic control of dissolution is possible, *i.e.*, an equally important influence of the surface mechanism and of the transport mechanism inside a diffusive boundary layer (DBL) close to the surface (see references below). The consequence of such a mixed kinetic control on the pattern of dissolution displayed in the plug-flow experiment will be discussed in Section 4.2.

4.1 Geometric and Reactive Surface Area of a Rock, at the Core Scale

Additionally to the analyses performed on the ENT1P sample, published experimental results were considered to extend the spectrum of lithologies and rock types in this

discussion. Intuitively it can be assumed that the reactive surface area will be in inverse relation with access to the pores. In Kieffer *et al.* (1999) and Jové Colón *et al.* (2004) the dissolution rate constant k of quartz grains mechanically extracted from a sediment, the Fontainebleau sandstone, was measured in a mixed-flow reactor, on a BET surface area basis. In the same conditions (80°C, basic solution, in order to obtain significant quartz dissolution) cores of the Fontainebleau sandstone were altered in a single-pass plug-flow percolation cell. The authors looked for the reactive surface area to be combined with the reaction rate constant (k) to account for the dissolution rate of the rocks. Moreover, taking advantage of a specific diagenetic feature displayed by the Fontainebleau sandstone (Thiry, 1999), they worked on a set of samples that exhibits a substantial range of porosity (Φ) values (5 to 17%). They were able to study the variation, with porosity, of a "specific reactive surface area", $\overline{S_r^0}$ (expressed in cm^{-1}), defined as the ratio between reactive surface area and rock volume in the initial (natural) state. Jové Colón *et al.* (2004) showed that the dissolution efficiency, and consequently the porosity enhancement during the flow-through experiment, increases with $\overline{S_r^0}$ (their Figure 3). However, the parameter $\overline{S_r^0}$ strongly depends on the composition and structure of the rock studied. Due to the presence of micrite grains in the ENT1P limestone it takes values that are much higher than those calculated for the Fontainebleau sandstone. Unfortunately, additional BET measurements after the flow-through episodes were not available for the present discussion.

Johnson *et al.* (1998) presented two experiments performed on a plug of packed sand grains, in a plug-flow reactor at 240°C. The discussion is limited to the first experiment, where the dissolution rate constant of quartz, compiled by Tester *et al.* (1994) on a BET surface area basis, was used to discuss the dissolution rate measured during the flow-through experiment. A BET surface area of 0.0509 m$^2 \cdot$g^{-1} was measured for the sand grains, such that the product of terms $\left[k_+(T)\right]_{\text{BET.}}^{\text{plug}} \cdot S_{\text{BET}}^{\text{grains}}$ the authors used is *ca.* 0.03 mol$\cdot$g$_{\text{quartz}}^{-1} \cdot$y^{-1}.

For modelling the plug-flow experiment described by Johnson *et al.* (1998) we considered values related to geometric surface instead of BET surface. We used a value of $\left[k_+(T)\right]_{\text{geom}} = 6.326$ mol$\cdot$m$^{-2} \cdot$y^{-1} for the dissolution rate constant of quartz, compiled by Tester *et al.* (1994) on a geometric surface area basis. From the grain size in the packed bed, an initial geometric surface area of 0.0229 m$^2 \cdot$g^{-1} was used in the DIAPHORE simulation, such that the product of terms $\left[k_+(T)\right]_{\text{geom}}^{\text{quartz}} \cdot S_{\text{geom}}^{\text{grains}}$ is *ca.* 0.145 mol$\cdot$g$_{\text{quartz}}^{-1} \cdot$y^{-1}.

We reproduced correctly the measured profile of dissolved silica when applying a corrective term of 0.25 (value of σ) to the surface area *(Fig. 7)*. Such a value closely coincides with the ratio between $\left[k_+(T)\right]_{\text{BET}}^{\text{plug}} \cdot S_{\text{BET}}^{\text{grains}}$ cited above and $\left[k_+(T)\right]_{\text{geom}}^{\text{quartz}} \cdot S_{\text{geom}}^{\text{grains}}$ used in DIAPHORE.

In conclusion, if it is assumed that the rock dissolution is governed by a surface mechanism, and if a model of sphere shaped grains is used to update the surface area considered in the dissolution rate law, then a correction parameter (σ) must be applied to this surface area to account for the rock fabric. The value of σ is lower than 1 and increases with porosity. It reflects the ease of access offered to the fluid that flows through the rock, to reach the faces of the mineral grains.
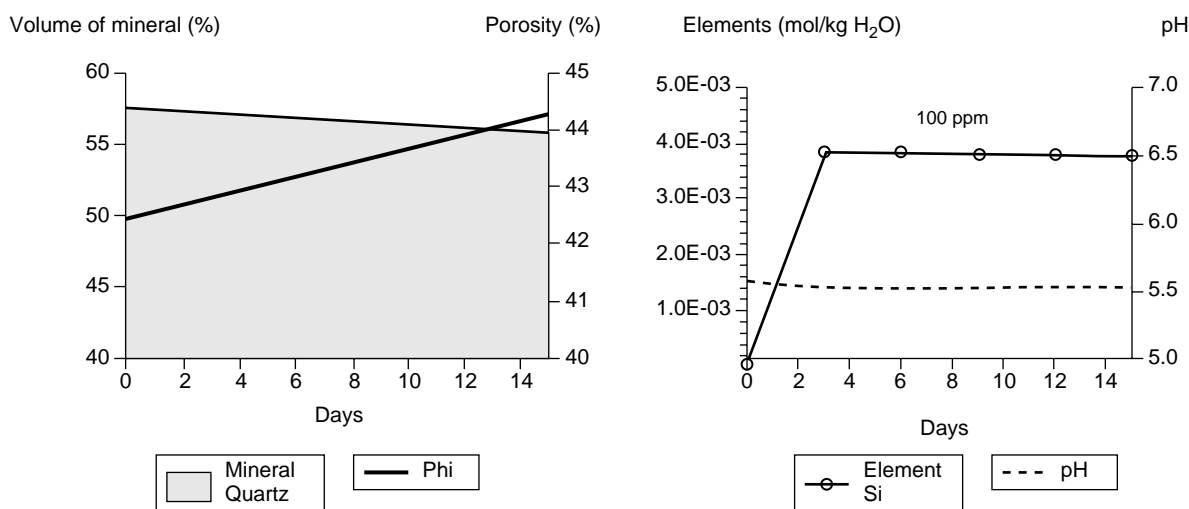

Figure 7

Simulation of the plug-flow experiment on quartz agregate presented by Johnson *et al.* (1998). Left side: the evolution of the agregate matrix. Right side: the evolution of dissolved silica at the outlet (line) and comparison with value measured in the effluent (circles).

4.2 Integration of a Diffusion Effect in the Kinetic Rate

In the preceding section it was assumed that the reaction rates are the same for separated minerals having a high water-to-mineral ratio, and for the rock system having a much lower water-to-mineral ratio and limited access to reactive surfaces. This assumption allowed the use of reaction rates determined from isolated minerals to estimate the reactive surface area available in the rock, as was done by Johnson *et al.* (1998), Kieffer *et al.* (1999) and Jové Colón *et al.* (2004) for the case of quartz dissolution, a process which is clearly surface controlled.

In the case of calcite at 25°C, however, several authors claimed that somewhere between pH 4 and pH 5 the kinetic control of dissolution becomes mixed, *i.e.*, a process controlled partly by the reaction at the mineral surface, partly by the diffusive transfer, in water close to the mineral surface, of aqueous species involved in the reaction (Rickard and Sjöberg, 1983; Sjöberg and Rickard, 1984). At pH < 3.5, Alkattan *et al.* (1998) showed that the control is diffusional. Obviously the diffusion (or transport) control varies also according to the hydrodynamic conditions.

The dissolution of a mineral results from a sequence of mechanisms, among which are the surface reaction and the diffusive transport of dissolved species in a boundary layer of the solution close to the mineral surface (DBL) (*e.g.*, Berner, 1978; Casey, 1987; Stumm and Wieland, 1990; Lasaga, 1998). The kinetics of dissolution is controlled by the slowest mechanism of the sequence. In case of a mixed control the kinetic rate constant which is directly measured depends on an apparent coefficient, noted k^*, that combines the effects of surface mechanism (k_s) and transport mechanism (k_t):

$$k^* = \frac{k_s \cdot k_t}{k_s + k_t} \qquad (8)$$

In the previous sections the difference between measured and modelled reaction rates was seen as the consequence of the simplistic grain representation used to derive the surface area involved in the reaction. We used the PWP model as a surface-controlled dissolution rate and the σ coefficient (0.15) as a corrective term to apply to the surface area. An alternative interpretation is to consider that the species activities have distinct values at the mineral surface and in the bulk solution and that the reaction rate is partly controlled by diffusion of species in pore water. In that case a mixed control is assumed for the dissolution rate, as in Equation (8). If we suppose that:

$$k^* = 0.15 \, k_s \qquad (9)$$

with k_s equal to the PWP dissolution rate, the k^* dissolution rate also fits the experimental results obtained on the crinoidal limestone. From Equations (8) and (9) can be derived a value for k_t, which depends on pH.

Using the relation:

$$\frac{k_t}{(\mathrm{H^+})} = \frac{D_{\mathrm{H^+}}}{\delta} \qquad (10)$$

and a value of 3.0×10^{-9} m²·s⁻¹ for $D_{\mathrm{H^+}}$, the molecular diffusion coefficient of the proton at 25°C (Alkattan *et al.*, 1998), the average thickness δ of the DBL ranges between 110 μm and 15 μm as pH ranges between 3.5 and 5, respectively.

Dreybrodt (1981) and later Buhmann and Dreybrodt (1985a, 1985b, 1987) introduced in a detailed way, a model for limestone dissolution close to the Earth surface, applicable to linear water conduits either in vadose zone (designed by "open system", *i.e.*, in contact with atmospheric CO₂) or in phreatic zone (designed by "closed system"). The important feature of this model is that it considers three possible controls of the whole reaction rate:

– the surface-controlled mechanism at the mineral-water interface, modelled by the PWP kinetics;
– the conversion of CO_2(aq) to H_2CO_3;
– the diffusive transport of the dissolved species in a diffusion layer.

The model was extended to porous media by Baumann *et al.* (1985) on the basis of experiments made on plugs of packed calcite grains.

The first and third controls of this model were considered above, through Equations (8) to (10). The second control of the Dreybrodt's group model, listed above, involves the kinetics of CO_2(aq) hydration in H_2CO_3 (and of the reverse reaction), which has been extensively described by Usdowski (1982). For the reaction:

$$CO_2(aq) \; \underset{k'}{\overset{k}{\rightleftarrows}} \; \Sigma C \qquad (11)$$
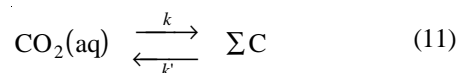
at 25°C and pH *ca.* 5, where ΣC represents the total dissolved carbon, the values of log k and log k' are close to -1.6 and to -1, respectively. Usdowski (1982) showed that in these conditions less than 10 s are necessary to reach a situation close (99%) to equilibrium in Reaction (11). From this result we concluded that it was possible to neglect this additional control in the process studied.

CONCLUSION

Provided adequate methodology is available to assess that the risk of leakage is limited, trapping CO_2 in deep saline aquifers and depleted hydrocarbon reservoirs will be one of the most accessible technical solutions able to contribute to a reduction of greenhouse-gas emissions. The prediction of CO_2 fate, either during injection or on the long term after injection, puts however a stressing demand for appropriate numerical models that must integrate, in particular, formalisms to represent the

rate of water-mineral reactions. The problem addressed in the present article concerns the way to use such reaction rates, measured from individual, well characterized minerals in well known hydrodynamic and geochemical conditions, for simulating reactions which involve the same minerals included in rocks or other porous materials. This problem is more generally met in any geo-engineering analysis, for the performance evaluation of underground installations where reaction-transport mechanisms are active. The results shown here, derived from an empirical comparison between experimental measurements on very simple plug-scale samples and simulations obtained with a reaction-transport code, indicate that the problem is far from being straightforward. A nonempirical approach would be to consider the mass-balance equations of the reaction-transport problem at the pore scale, and to integrate them at the scale of a representative elementary volume (a scale where the Darcy's law would be used), using a methodology developed for instance by Quintard and Whitaker (1999). This approach is beyond the scope of the present paper.

Here the case of calcite and limestone was examined. If the control of the reaction is assumed to be the surface mechanism, as in the PWP model, it is convenient to deduce the reactive surface area of the rock from a geometric surface area, easily computed from a grain model. A coefficient must be applied to reduce the value of the geometric surface area. According to rock type, this coefficient varies between 0.1 and 1. Unfortunately, it is not a simple function of porosity. In contrast, in the considered range of low pH and high flow-rate values, the control of the reaction can be considered as mixed for calcite, or even driven by a diffusion mechanism. In that case an average thickness of the boundary layer allows to put a lower limit on the reaction rate. In both cases, at the scale considered, the dissolution rate of the sediment can be bounded by values which are in a reasonable range (one order of magnitude).

ACKNOWLEDGEMENTS

REFERENCES

Alkattan, M., Oelkers, E.H., Dandurand, J.L. and Schott, J. (1998) An Experimental Study of Calcite and Limestone Dissolution Rates as a Function of pH from –1 to 3 and Temperature from 25 to 80°C. *Chem. Geol.*, 151, 199-214.

Bachu, S., Gunter, W.D. and Perkins, E.H. (1994) Aquifer Disposal of CO_2: Hydrodynamic and Mineral Trapping. *Energy Convers. Mgmt.*, 35, 269-279.

Baumann, J., Buhmann, D., Dreybrodt, W. and Schulz, H.D. (1985) Calcite Dissolution Kinetics in Porous Media. *Chem. Geol.*, 53, 219-228.

Berner, R.A. (1978) Rate Control of Mineral Dissolution under Earth Surface Conditions. *Am. Jour. Sci.*, 278, 1235-1252.

Brunauer, S., Emmett, P.H. and Teller, E. (1938) Adsorption of Gases in Multimolecular Layers. *Jour. Am. Chem. Soc.*, 60, 309-319.

Buhmann, D. and Dreybrodt, W. (1985a) The Kinetics of Calcite Dissolution and Precipitation in Geologically Relevant Situations of Karst Areas. 1. Open System. *Chem. Geol.*, 48, 189-211.

Buhmann, D. and Dreybrodt, W. (1985b) The Kinetics of Calcite Dissolution and Precipitation in Geologically Relevant Situations of Karst Areas. 2. Closed System. *Chem. Geol.*, 53, 109-124.

Buhmann, D. and Dreybrodt, W. (1987) Calcite Dissolution in the System H_2O-CO_2-$CaCO_3$ with Participation of Foreign Ions. *Chem. Geol.*, 64, 89-102.

Burch, T.E., Nagy, K.L. and Lasaga, A.C. (1993) Free Energy Dependence of Albite Dissolution Kinetics at 80°C and pH 8.8. *Chem. Geol.*, 105, 137-162.

Busenberg, E. and Plummer, L.N. (1986) A Comparative Study of the Dissolution and Crystal Growth Kinetics of Calcite and Aragonite. In: *Studies in Diagenesis*, F.A. Mumpton (Ed.), *USGS Bull.*, 1578, 139-168.

Casey, W.H. (1987) Heterogeneous Kinetics and Diffusion Boundary Layers: the Example of Reaction in Fracture. *Jour. Geophys. Res.*, 92, 8007-8013.

Cassou, C. (2000) Modélisation numérique des interactions eau-roche. *Thèse*, université de Bordeaux.

Chou, L. and Wollast, R. (1985) Steady State Kinetics and Dissolution Mechanisms of Albite. *Amer. Jour. Sci.*, 285, 963-993.

Chung, F.T.H., Jones, R.A. and Nguyen, T.H. (1988) Measurements and Correlations of the Physical Properties of CO_2-Heavy Crude Oil Mixtures. *SPE Reservoir Engineering*, 3, 822-828.

Coudrain-Ribstein, A., Gouze, P. and de Marsily, G. (1998) Temperature - Carbon Dioxide Partial Pressure Trends in Confined Aquifers. *Chem. Geol.*, **145**, 73-89.

Devidal, J.L., Schott, J. and Dandurand, J.L. (1997) An Experimental Study of Kaolinite Dissolution and Precipitation Kinetics as a Function of Chemical Affinity and Solution Composition at 150°C, 40 bar, and pH 2, 6.8 and 7.8. *Geoch. Cosmoch. Acta*, 61, 5165-5186.

Dove, P.M. and Crerar, D.A. (1990) Kinetics of Quartz Dissolution in Electrolyte Solutions Using a Hydrothermal Mixed-Flow Reactor. *Geoch. Cosmoch. Acta*, 54, 955-969.

Drever, J.I. (1997) *The Geochemistry of Natural Waters. Surface and Groundwater Environments*, 3rd ed., Prentice-Hall, New Jersey.

Dreybrodt, W. (1981) Kinetics of the Dissolution of Calcite and its Application to Karstification. *Chem. Geol.*, 31, 245-269.

Dromgoole, E.L. and Walter, L.M. (1990) Inhibition of Calcite Growth Rates by Mn^{2+} in $CaCl_2$ Solutions at 10, 25 and 50°C. *Geoch. Cosmoch. Acta*, 54, 2991-3000.

Duan, Z. and Sun, R. (2003) An Improved Model Calculating CO_2 Solubility in Pure Water and Aqueous NaCl Solutions from 273 to 533 K and from 0 to 2000 bar. *Chem. Geol.*, 193, 257-271.

Eisenlohr, L., Meteva, K., Gabrovšek, F. and Dreybrodt, W. (1999) The Inhibiting Action of Intrinsic Impurities in Natural

Calcium Carbonate Minerals to their Dissolution Kinetics in Aqueous H_2O-CO_2 Solutions. *Geoch. Cosmoch., Acta*, 63, 989-1002.

Enick, R.M. and Klara, S.M. (1990) CO_2 Solubility in Water and Brine under Reservoir Conditions. *Chem. Eng. Comm.*, 90, 23-33.

Gautier, J.M., Oelkers, E.H. and Schott, J. (2001) Are Quartz Dissolution Rates Proportional to BET Surface Areas? *Geoch. Cosmoch. Acta*, 65, 1059-1070.

Gunter, W.D., Perkins, E.H. and McCann, T.J. (1993) Aquifer Disposal of CO_2-Rich Gases: Reaction Design for Added Capacity. *Energy Convers. Mgmt.*, 34, 941-948.

Gunter, W.D., Wiwchar, B. and Perkins, E.H. (1997) Aquifer Disposal of CO_2-Rich Greenhouse Gases: Extension of the Time Scale of Experiment for CO_2-Sequestering Reactions by Geochemical Modelling. *Mineral. and Petrol.*, 59, 121-140.

Guy, C. and Schott, J. (1989) Multisite Surface Reaction *versus* Transport Control During the Hydrolysis of a Complex Oxide. *Chem. Geol.*, 78, 181-204.

Helgeson, H.C. (1969) Thermodynamics of Hydrothermal Systems at Elevated Temperatures and Pressures. *Amer. Jour. Science*, 267, 729-804.

Helgeson, H.C., Kirkham, D.H. and Flowers, G.C. (1981) Theoretical Prediction of the Thermodynamic Behavior of Aqueous Electrolytes by High Pressures and Temperatures. IV. Calculation of Activity Coefficients, Osmotic Coefficients, and Apparent Molal and Standard and Relative Partial Molal Properties to 600°C and 5 kb. *Am. Jour. of Science*, 281, 1249-1516.

Helgeson, H.C., Murphy, W.M. and Aagaard, P. (1984) Thermodynamic and Kinetic Constraints on Reaction Rates Among Minerals and Aqueous Solutions. II. Rate Constants, Effective Surface Area, and the Hydrolysis of Feldspar. *Geoch. Cosmoch. Acta*, 48, 2405-2432.

Hutcheon, I. and Abercrombie, H. (1990) Carbon Dioxide in Clastic Rocks and Silicate Hydrolysis. *Geology*, **18**, 541-544.

Jeschke, A.A. and Dreybrodt, W. (2002) Dissolution Rates of Minerals and their Relation to Surface Morphology. *Geoch. Cosmoch. Acta*, 66, 3055-3062.

Johnson, J.W., Knauss, K.G., Glassley, W.E., DeLoach, L.D. and Tompson, A.F.B. (1998) Reactive Transport Modeling of Plug-Flow Reactor Experiments: Quartz and Tuff Dissolution at 240°C. *Jour. of Hydrol.*, 209, 81-111.

Johnson, J.W., Nitao, J.K. and Knaus, K.G. (2004) Reactive Transport Modelling of CO_2 Storages in Saline Aquifers to Elucidate Fundamental Processes, Trapping Mechanisms, and Sequestration Partitioning. In: *Geological Storage of Carbon Dioxide*, S.J. Baines and R.H. Worden (Eds.), Geol. Soc. Spec. Publ. 233, London.

Jové Colón, C.F., Oelkers, E.H. and Schott, J. (2004) Experimental Investigation of the Effect of Dissolution on Sandstone Permeability, Porosity, and Reactive Surface Area. *Geoch. Cosmoch. Acta*, 68, 805-817.

Kervévan, C., Azaroual, M. and Durst, P. (2005) Improvement of the Calculation Accuracy of Acid Gas Solubility in Deep Reservoir Brines: Application to the Geological Storage of CO_2. *This Issue*.

Kieffer, B., Jové Colón, C.F., Oelkers, E.H. and Schott, J. (1999) An Experimental Study of the Reactive Surface Area of the Fontainebleau Sandstone as a Function of Porosity, Permeability, and Fluid Flow Rate. *Geoch. Cosmoch. Acta*, 63, 3525-3534.

Knapp, R.B. (1989) Spatial and Temporal Scales of Local Equilibrium in Dynamic Fluid-Rock systems. *Geoch. Cosmoch. Acta*, 53, 1955-1964.

Lasaga, A.C. (1998) Kinetic Theory in the Earth Sciences. Princeton University Press.

Le Gallo, Y., Bildstein, O. and Brosse, E. (1998) Coupled Reaction-Flow Modeling of Diagenetic Changes in Reservoir Permeability, Porosity and Mineral Compositions. *Jour. of Hydrology*, 209, 366-388.

Lichtner, P.C. (1996) Continuum Formulation of Multicomponent-Multiphase Reactive Transport. In: *Reactive Transport in Porous Media*, Lichtner, P.C., Steefel, C.I. and Oelkers, E.H. (Eds.), Mineral Society of America, *Reviews in Mineralogy,* 34, 1-81.

Lüttge, A., Winkler, U. and Lasaga, A.C. (2003) Interferometric Study of the Dolomite Dissolution: A New Conceptual Model for Mineral Dissolution. *Geoch. Cosmoch. Acta*, 67, 1099-1116.

Mast, M.A. and Drever, J.I. (1987) The Effect of Oxalate on the Dissolution Rates of Oligoclase and Tremolite. *Geoch. Cosmoch. Acta*, 51, 2559-2568.

Mathis, R.L. and Sears, S.O. (1984) Effect of CO_2 Flooding on Dolomite Reservoir Rock, Denver unit, Wasson (San Andres) Field, TX. *SPE 13132*.

Murphy, W.M. and Helgeson, H.C. (1989) Thermodynamic and Kinetic Constraints on Reaction Rates Among Minerals and Aqueous Solutions. IV. Retrieval of Rate Constants and Activation Parameters for the Hydrolysis of Pyroxene, Wollastonite, Olivine, Andalusite, Quartz and Nepheline. *Am. Jour. of Science*, 289, 17-101.

Nagy, K.L. and Lasaga, A.C. (1992) Dissolution and Precipitation Kinetics of Gibbsite at 80°C and pH 3: The Dependence on Solution Saturation State. *Geoch. Cosmoch. Acta*, 56, 3093-3111.

Nagy, K.L., Steefel, C.I., Blum, A.E. and Lasaga, A.C. (1990) Dissolution and Precipitation Kinetics of Kaolinite: Initial Results at 80°C with Application to Porosity Evolution in a Sandstone. In: *Prediction of Reservoir Quality Through Reservoir Modeling*, I.D. Meshri and P.J. Ortoleva (Eds.), *AAPG Mem.* 49, 85-101.

Nagy, K.L., Blum, A.E. and Lasaga, A.C. (1991) Dissolution and Precipitation Kinetics of Kaolinite at 80°C and pH 3: The Dependence on Solution Saturation State. *Am. Jour. of Science*, 291, 649-686.

Noiriel, C., Bernard, D., Gouze, P. and Thibault, X. (2005) Hydraulic Properties and Microgeometry Evolution Accompanying Limestone Dissolution by Acidic Water. *This Issue*.

Oelkers, E.H. (1996) Physical and Chemical Properties of Rocks and Fluids for Chemical Mass Transport Calculations. In: *Reactive Transport in Porous Media*, P.C. Lichtner, C.I. Steefel, E.H. Oelkers (Eds.), Mineral Society of America, *Reviews in Mineralogy*, 34, 131-191.

Plummer, L.N., Wigley, T.M.L. and Parkhurst, D.L. (1978) The Kinetics of Calcite Dissolution in CO_2-Water Systems at 5° to 60°C and 0.0 to 1.0 atm CO_2. *Am. Jour. Sci.*, 278, 179-216.

Pokrovsky, O.S. and Schott, J. (2002) Surface Chemistry and Dissolution Kinetics of Divalent Metal Carbonates. *Environ. Sci. Technol.*, 36, 426-432.

Portier, S. (2005). Solubilité de CO_2 dans les saumures des bassins sédimentaires. Application au stockage de CO_2. *Thèse*, univ. de Strasbourg.

Portier, S. and Rochelle, C. (2005) Modelling CO_2 Solubility in Pure Water and NaCl-Type Waters from 0 to 300 Degrees Celcius and from 1 to 300 bar. Application to the Utsira Formation at Sleipner. In: *Geochemical Aspects of CO_2 Sequestering*, Special Issue of *Chemical Geology*, in press.

Quintard, M. and Whitaker, S. (1999) Dissolution of an Immobile Phase During Flow in Porous media. *Industrial and Engineering Chemistry Research*, 38, 833-844.

Rickard, D.T. and Sjöberg, E.L. (1983) Mixed Kinetic Control of Calcite Dissolution Rates. *Amer. Jour. Science*, 283, 815-830.

Ross, G.D., Todd, A.C., Tweedie, J.A. and Will, A.G.S. (1982) The Dissolution Effects of CO_2-Brine Systems on the Permeability of UK and North Sea Calcareous Sandstones. *SPE/DOE* 10685.

Schnoor, J.L. (1990) Kinetics of Chemical Weathering: a Comparison of Laboratory and Field Weathering Rates. In: *Aquatic Chemical Kinetics*, W. Stumm (Ed.), Wiley-Interscience Publ., 475-504.

Simon, R. and Graue, D. (1965) Generalized Correlations for Predicting Solubility, Swelling and Viscosity Behavior of CO_2-Crude Oil System. *J. Petrol. Tech.*, 102-106.

Sjöberg, E.L. and Rickard, D.T. (1984) Temperature Dependence of Calcite Dissolution Kinetics between 1 and 62°C at pH 2.7 to 8.4 in Aqueous Solutions. *Geoch. Cosmoch. Acta*, 48, 485-493.

Smith, J.T. and Ehrenberg, S.N. (1989) Correlation of Carbon Dioxide Abundance with Temperature in Clastic Hydrocarbon Reservoirs: Relationship to Inorganic Chemical Equilibrium. *Mar. & Petrol. Geol.,* 6, 129-135.

Steefel, C.I. and MacQuarrie, K.T.B. (1996) Approaches to Modeling Reactive Transport in Porous Media. In: *Reactive Transport in Porous Media*, Lichtner, P.C., Steefel, C.I., Oelkers, E.H. (Eds.), Mineral Society of America, *Reviews in Mineralogy*, 34, 83-129.

Stumm, W. and Morgan, J.J. (1970) *Aquatic Chemistry*. Wiley-Interscience, New York, London, Sidney, Toronto.

Stumm, W. and Wieland, E. (1990) Dissolution of Oxide and Silicate Minerals: Rates Depend on Surface Speciation. In: *Aquatic Mineral Kinetics, Reaction Rates of Processes in Natural Waters*, W. Stumm (Ed.), 367-400.

Svec, R.K. and Grigg, R.B. (2001) Physical Effects of WAG Fluids on Carbonate Core Plugs. *SPE 71496.*

Tester, J.W., Worley, W.G., Robinson, B.A., Grigsby, C.O. and Feerer, J.L. (1994) Correlating Quartz Dissolution Kinetics in Pure Water from 25 to 625°C. *Geoch. Cosmoch. Acta*, 58, 2407-2420.

Thiry, M. (1999) Diversity of Continental Silicification Features: Examples from the Cenozoic Deposits in the Paris Basin and Neighbouring Basement. *Int. Ass. Sediment. Spec. Publ.*, 27, 87-127.

Usdowski, E. (1982) Reactions and Equilibria in the Systems CO_2-H_2O and $CaCO_3$-CO_2-H_2O (0-50°C). A Review. *N. Jb. Miner. Abh.*, 144, 2, 148-171.

Van Cappellen, P., Charlet, L., Stumm, W. and Wersin, P. (1993) A Surface Complexation Model of the Carbonate Mineral-Aqueous Solution Interface. *Geoch. Cosmoch. Acta*, 57, 3505-3518.

Vengu, T. (1983) Propriétés thermodynamiques d'un pétrole brut en présence de gaz carbonique. Application à la récupération assistée. *Thèse*, univ. Paris VI.

White, A.F. and Brantley, S.L. (2003) The Effect of Time on the Weathering of Silicate Minerals: Why Do Weathering Rates Differ in the Laboratory and Field? *Chem. Geol.*, 202, 479-506.

Withe, A.F. and Peterson, M. (1990) The Role of Reactive Surface Areas in Chemical Weathering. In: *Geochemistry of the Earth's Surface and of Mineral Formation*, 2nd Int. Symp., July 2-8 1990, Aix-en-Provence, France, 334-338.

Xu, T., Apps, J.A. and Pruess, K. (2003) Reactive Geochemical Transport Simulation to Study Mineral Trapping for CO_2 Disposal in Deep Arenaceous Formations. *Jour. Geophys. Res.*, 108, B2 (in press).

APPENDIX A

FORMALISM USED IN THE GEOCHEMICAL MODEL FOR REPRESENTING REACTION RATES

The formalism is derived from the transition state theory (*e.g.*, Helgeson *et al.*, 1984; Murphy and Helgeson, 1989; Lasaga, 1998), with the restrictions that only H$^+$ and OH$^-$ participate to the elaboration of the activated complex, and that the Temkin's coefficient is 1.

For dissolution the rate R_d (mol·m$^{-1}_{solution}$ ·y^{-1}) is written:

$$R_d = -k_+(T) \cdot S_r \cdot \left(1 - \frac{Q}{K^T_{eq}}\right) \qquad (A1)$$

where $k_+(T)$ (mol·m$^{-2}_{mineral}$ ·y^{-1}) is the rate constant at fixed T and pH, S_r (m$^2_{mineral}$ ·l$^{-1}_{solution}$) is the reactive surface area per litre of solution, $\left(1 - \dfrac{Q}{K^T_{eq}}\right)$ (noted also 1-Ω) is the departure from equilibrium.

For any value of temperature (T) $k_+(T)$ is expressed as a function of pH considering three domains, respectively acid, neutral and basic. In the acid domain:

$$k_+(T) = k^T_{d,A} \cdot \left(H^+\right)^{n^T_A} \qquad (A2)$$

where (H$^+$) is the proton activity, n^T_A is the order of the reaction, $k^T_{d,A}$ is a kinetic coefficient that depends on T.

In the neutral domain:

$$k_+(T) = k^T_{d,N} \qquad (A3)$$

In the basic domain:

$$k_+(T) = k^T_{d,B} \cdot (OH^-)^{n^T_B} \qquad (A4)$$

where notations are equivalent to those used in Equation (A2).

The values pH^T_A and pH^T_B that limit the domains of pH depend on the mineral and, more weakly, on T. The parameters pH^T_A, pH^T_B, n^T_A, n^T_B, $k^T_{d,A}$, $k^T_{d,N}$ and $k^T_{d,B}$ (non independent) are chosen by the model's user according to the experimental data published in literature for the conditions of interest.

The kinetic constant depends on temperature according to the Arrhenius'law (to be applied eventually in a limited range of pH values):

$$k^T_{d,pH} = k^*_{d,pH} \cdot \exp\left(-\frac{(E^*_a)_{d,pH}}{RT}\right) \qquad (A5)$$

where $k^T_{d,pH}$ represents $k^T_{d,A}$, $k^T_{d,N}$ or $k^T_{d,B}$ (depending on the considered pH domain), $(E^*_a)_{d,pH}$ (J·mol^{-1}) is an apparent activation energy (apparent because the kinetic mechanism is not elementary in general), $k^*_{d,pH}$ is a pre-exponential factor, R is a contant (8.3143 J·mol^{-1}·K^{-1}).

For precipitation two steps are considered, nucleation and growth. Nucleation is represented by an empirical over-saturation threshold value, that has to be overcome before crystal growth can take place. The rate of mineral growth R_p (mol·m$^{-1}_{solution}$ ·y^{-1}) is represented in the following way:

$$R_p = k_-(T) \cdot S_r \cdot \left[\left(\frac{Q}{K^T_{eq}}\right)^{a_T} - 1\right]^{b_T} \qquad (A6)$$

where $k_-(T)$ (mol·m$^{-2}_{mineral}$ ·y^{-1}) is the rate constant for precipitation at temperature T, a_T et b_T are empirical coefficients. Here again, the parameter values are adjusted by the model's user to fit experimental data considered as relevant for the case study.

In the same way the kinetic rate depends on T according to the Arrhenius' law:

$$k_-(T) = k^*_p \cdot \exp\left(-\frac{(E^*_a)_p}{RT}\right) \qquad (A7)$$

where $(E^*_a)_p$ is an apparent activation energy and k^*_p a pre-exponential factor. It is extremely rare to find enough experimental data in literature to be able to adjust Equation (A7).

Kinetic theory is now dealing with surface complexation to describe the reaction rates, and the concept of activated complex is declining. For oxides surface complexation is dominated by proton exchanges and the formalisms developed above can be adapted, at least in well specified conditions, without too much difficulties. For carbonates surface complexation is governed by a larger diversity of ionic exchanges (*e.g.*, Van Cappellen *et al.*, 1993; Pokrovsky and Schott, 2002). It explains why the formulae giving carbonate kinetic rates, *e.g.*, in the PWP model, were often relatively complex expressions of the solution composition.